

Magnetic and ferroelectric phase diagram of twisted CrI_3 layers

Haoshen Ye and Shuai Dong*

*Key Laboratory of Quantum Materials and Devices of Ministry of Education,
School of Physics, Southeast University, Nanjing 21189, China*

(Dated: July 17, 2025)

Twisting layers provide a rich ore for exotic physics in low dimensions. Despite the abundant discoveries of twistrionics from the aspect of electronic structures, ferroic moiré textures are more plain and thus less concerned. Rigid lattice models are straightforward which can give a rough but intuitional description in most cases. However, taking CrI_3 as a model system, here we will demonstrate that the interlayer stacking potential can spontaneously lead to structural relaxation, which plays a vital role to understand the ferroicity in the twisted superlattices. The magnetic ground state is sensitive to the stacking mode and twisting angles, which can be seriously affected by the structural relaxation. In particular, the expected magnetic bubbles are annihilated in its bilayer. In contrast, due to topological protection, the ferroelectric vortices are more robust to structural relaxation, as well as twisting angle and thickness. Due to the universal existence of spontaneous structural relaxation in twisted superlattices, our work may lead to a general revisitation of emerging physics of twistrionics.

Magnets and ferroelectrics are key functional materials widely used in technological applications. The rise of van der Waals (vdW) materials opens new avenues for realizing magnetism and ferroelectricity in reduced dimensions [1–5]. The weak interlayer interactions make these vdW multilayers highly tunable, which allows for the manipulations of their electronic, magnetic, and ferroelectric properties through external stimuli [6–10]. Such tunability paves the way for novel applications with versatile quantum functionalities [11–14].

Twist engineering, by creating angle mismatch between adjacent vdW layers, has been found to be a rich ore of exotic physics, such as ultra-flat bands, topological polaritons, as well as unconventional superconductivity [15–17]. Besides these holistic effects, the periodic variation of stacking modes will induce spatial modulation of magnetism, ferroelectricity, as well as optical response in twisted superlattices [18–22]. In fact, a twisted superlattice can be understood as a mosaic of local stacking modes [5, 23–25]. Due to the one-to-one correspondence between the stacking mode and some physical properties, one can naturally expect the formation of periodic ferroic domains in these twisted superlattices, providing an ideal platform to study and manipulate the ferroic functionalities of domains and domain walls [26, 27].

Another consequence of twisting is that the local stacking energy is also periodically modulated. To reduce the stacking energy, structural relaxation will be inevitable, which has been experimentally evidenced in twisted superlattices [28–31]. However, its effects to magnetism and ferroelectricity in twisted vdW superlattices have been mostly ignored, while simplified rigid lattices are usually modeled to describe these twisted layers [25–27]. Then an essential question is that whether the structural relaxation is vital to the ferroic physics in twisting layers, or it is indeed negligible as done before. This issue should be

solved before the next step of twistrionics with ferroicity involved.

In this Letter, we will clarify the key role of structural relaxation to magnetism and ferroelectricity in twisted CrI_3 superlattices, going beyond the rigid model. On one hand, the magnetic texture of twisted CrI_3 layers is found to be significantly affected by the structural relaxation, which can fully suppress the magnetic bubbles in the CrI_3 bilayer with small twisting angles. On the other hand, although the ferroelectric domain walls are also seriously squeezed, the ferroelectric vortices survive after the structural relaxation, due to the topological protection. These results solve the discrepancy between prior experimental observations and theoretical expectations [26, 27, 32], providing a complete description of ferroicity in twisted materials.

As one of the earliest two-dimensional (2D) ferromagnets confirmed in experiment [1], CrI_3 has received numerous attentions and become the most studied 2D magnet. Interestingly, the sign of its interlayer magnetic coupling depends on the stacking mode [9], and sliding ferroelectricity is also expectable by tuning the stacking modes [33]. These stacking-dependent ferroic properties make twisted CrI_3 a perfect model system for studying the effects of structural relaxation to ferroicity in twisted superlattices.

Let's start from the simplest case: the CrI_3 1 + 1 bilayer. As illustrated in Fig. 1(a), the AA stacking mode can be transformed to the AB (or BA) mode by laterally sliding the top layer along $(1\bar{1}0)$ by $-1/3$ (or $1/3$) in fractional coordinate. By sliding along (110) by $-1/3$ and $1/3$, one can obtain the AC and CA stacking modes, respectively. In fact, the AB/BA and AC modes correspond to the low-temperature rhombohedral (R) and high-temperature monoclinic (M) phases of bulk CrI_3 [34]. The stacking energy landscape of sliding operation can be obtained via density functional theory (DFT) calculation [see EM1 in End Matter (EM)], which is consistent with previous studies [33, 35]. The details of

* sdong@seu.edu.cn

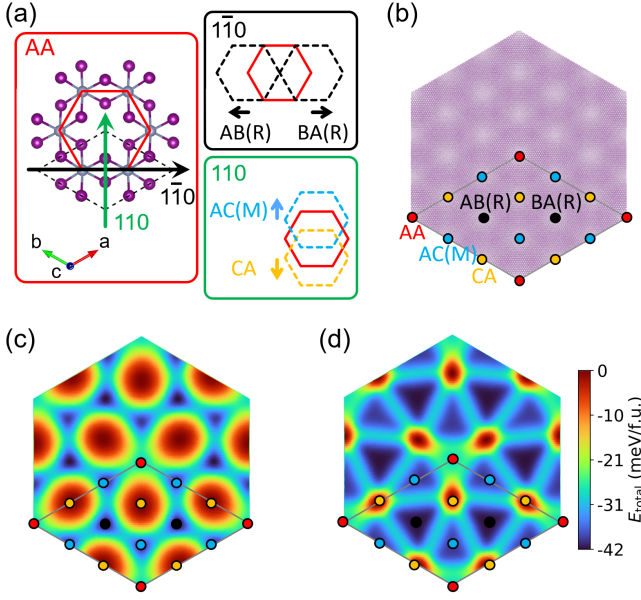


FIG. 1. The 1 + 1 CrI₃ bilayer. (a) Typical stacking modes obtained by interlayer sliding. (b) Atomic structure of the $\theta_{\text{twist}} = 0.99^\circ$ rigidly twisted case. Rhomb with broken lines: the minimum supercell. Color dots: the special positions corresponding to particular stacking modes. (c-d) Total energy (E_{total}) landscapes of the $\theta_{\text{twist}} = 0.99^\circ$ case: (c) without and (d) with structural relaxation.

DFT calculations can be found in Supplemental Materials (SM) [36].

As aforementioned, the twisting operation, characterized by the twisting angle θ_{twist} , can tune the stacking degree of freedom. For example, a $\theta_{\text{twist}} = 0.99^\circ$ twisting of CrI₃ bilayer leads to a supercell containing 13468 formula units, as Fig. 1(b). The typical stacking modes can also be evidenced locally in the twisted bilayer. The CrI₃ monolayer belongs to the space group $P\bar{3}1m$, which contains the three-fold rotation (C_{3z}) and vertical mirror (σ_v) symmetries. The C_{3z} symmetry ensures that every 120° rotation is equivalent to 0° . The σ_v symmetry makes the mirror-symmetric atomic positions of clockwise and anti-clockwise rotation by same angles relative to 0° . Consequently, the study of $\theta_{\text{twist}} \in [0^\circ, 60^\circ]$ captures all physics for twisted CrI₃ bilayer.

For the twisting mode shown in Fig. 1(b), the distribution of stacking energy E_{stack} can be mapped to Fig. 1(c). The gradient of stacking energy leads to intrinsic strain and stress, which will lead to spontaneous structural relaxation till the balance between E_{stack} and the strain energy E_{strain} . E_{strain} can be expressed as:

$$E_{\text{strain}} = \frac{1}{2} \sum_{ij} C_{ij} \varepsilon_{ij}^2, \quad (1)$$

where C and ε are the elastic tensor and strain tensor, respectively. i/j are coordinate axes. The value of C can be obtained via DFT calculation (Fig. S2 (a) and Table S1 in SM) [36].

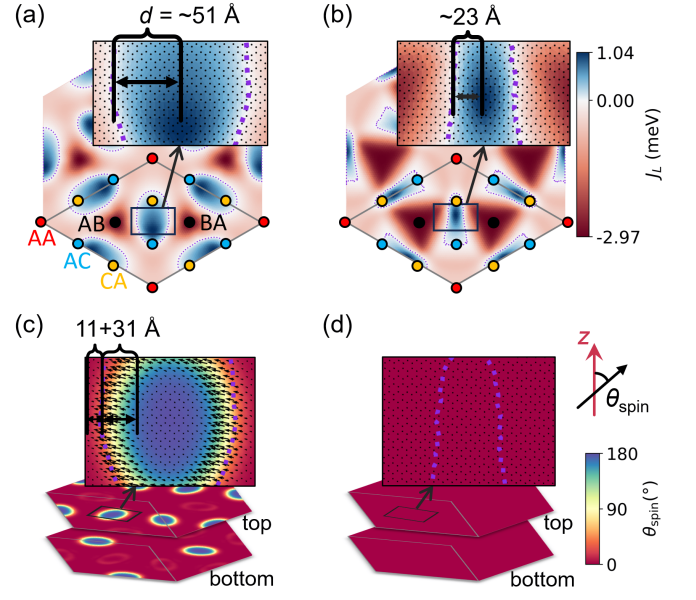


FIG. 2. Contour maps of interlayer magnetic coupling of $\theta_{\text{twist}} = 0.99^\circ$ 1 + 1 CrI₃ bilayers: (a) without and (b) with structural relaxation. Negative and positive values of J_L denote ferromagnetic and antiferromagnetic interactions. Corresponding magnetic textures: (c) without and (d) with structural relaxation. θ_{spin} : the polar angle of spin as the inset illustrates. Purple broken curve: the $J_L = 0$ boundary.

By minimizing the total energy $E_{\text{total}} = E_{\text{strain}} + E_{\text{stack}}$, the relaxation can be numerically simulated (see EM1 for details). As shown in Fig. 1(d), the CA regions with high E_{stack} profile seriously shrink to accommodate more R-phase and M-phase domains which are more energetically favorable. For the $\theta_{\text{twist}} = 0.99^\circ$ case, the total energy of CrI₃ bilayer is reduced by 9.85 meV/f.u. (ΔE_{stack} : -9.94 meV/f.u. & ΔE_{strain} : +0.09 meV/f.u.) from the structural relaxation, which is only 11.87 meV/f.u. higher than the lowest-energy AB/BA stackings. The increased E_{strain} comes from the strain accumulation at domain walls (see Figs. S3 and S4 in SM [36]). This relaxation is weakened in larger θ_{twist} cases with smaller supercells and domains. While in smaller θ_{twist} cases with larger supercells and domains, the width of stacking domain walls eventually stabilizes at an optimal value ($\sim 97 \pm 1$ Å).

For CrI₃, the sign of interlayer magnetic coupling (J_L) is sensitive to the stacking mode [33, 35]. As shown in Fig. 2(a), the elliptic regions with AC/CA-like stacking favor the antiferromagnetic coupling, while the AB/BA-like regions strongly favor the ferromagnetic coupling. The spatial modulation of J_L 's sign in this twisted bilayer creates magnetic competition around the transition boundary, which have been reported as a promising platform for magnetic bubbles (and merons) [37, 38]. Comparing with the pristine case, the antiferromagnetically-preferred regions are seriously shrunk [Fig. 2(b)] after the structural relaxation, which may affect the stabil-

ity of domain walls. In fact, sufficient space is required to accommodate the magnetic domain walls, otherwise, magnetic bubbles can not survive.

To estimate the width of magnetic domain walls and analyze the spin textures in the twisted CrI_3 bilayer, micromagnetic simulations based on the Landau-Lifshitz-Gilbert (LLG) equation is performed (see EM2 for details). As shown in Fig. 2(c), an elliptic magnetic bubble is formed at each antiferromagnetic J_L region, where spins are 180° flipped cross the magnetic domain wall with a width of ~ 42 Å in the rigidly twisted CrI_3 bilayer. By deducting the distance from the $J_L = 0$ boundary to the domain wall boundary (~ 11 Å), the required half-width (d) of the antiferromagnetic J_L region should be wider than 31 Å to meet the space requirement of forming a magnetic bubble in the rigidly twisted CrI_3 . As expected, for the relaxed structure, the $J_L > 0$ region is too narrow to host any magnetic bubble, as shown Fig. 2(d).

Then a following question is that whether any magnetic bubble can survive by tuning the twisting, e.g. θ_{twist} and layer thickness. To clarify this issue, we start from the rigidly twisted model. According to the direct geometric triangulation, the half-width d_{rigid} of antiferromagnetic J_L region in the rigidly twisted 1 + 1 CrI_3 bilayer can be estimated as:

$$d_{\text{rigid}} = \frac{D}{2} \sin^{-1}\left(\frac{\theta_{\text{twist}}}{2}\right), \quad (2)$$

where the scaling factor $D = 0.88$ Å (see EM3 for details). As shown in Fig. 3(a), the analytic Eq. 2 indeed matches the numerical solution of unrelaxed 1+1 CrI_3 bilayer. θ_{twist} should be less than 1.54° to provide enough d (> 31 Å) to accommodate magnetic bubbles in the rigidly twisted 1 + 1 CrI_3 bilayer. This estimation is consistent well with our numerical simulations (see Fig. S6 [36]).

After the structural relaxation, the real d is always smaller than 31 Å for any θ_{twist} , which reaches a saturation value (~ 23 Å) in the small θ_{twist} limit. This result solves the puzzle that why there is no magnetic bubbles observed in the twisted 1 + 1 CrI_3 bilayer [32], and predicts that it will never be while it should appear in the small θ_{twist} 's cases according to the rigid model.

In the large θ_{twist} limit, the supercell becomes smaller and smaller, which leads to smaller modulation periods and thus smaller d . Then the structural relaxation will be gradually suppressed, since the energy gain of E_{stack} from relaxation becomes meager to compensate the rapid increasing of E_{strain} (Fig. S2 in SM [36]). Indeed, when $\theta_{\text{twist}} > 2.65^\circ$, the simulated d is close to d_{rigid} .

Above study has demonstrated that the structural relaxation is disadvantage for the appearance of magnetic bubble. A straightforward way to suppress the structural relaxation is to tune the balance between E_{stack} and E_{strain} . A simple way is to use thicker twisting layers, in which the effective elastic stiffness will be significantly enhanced. Then the structural relaxation will become

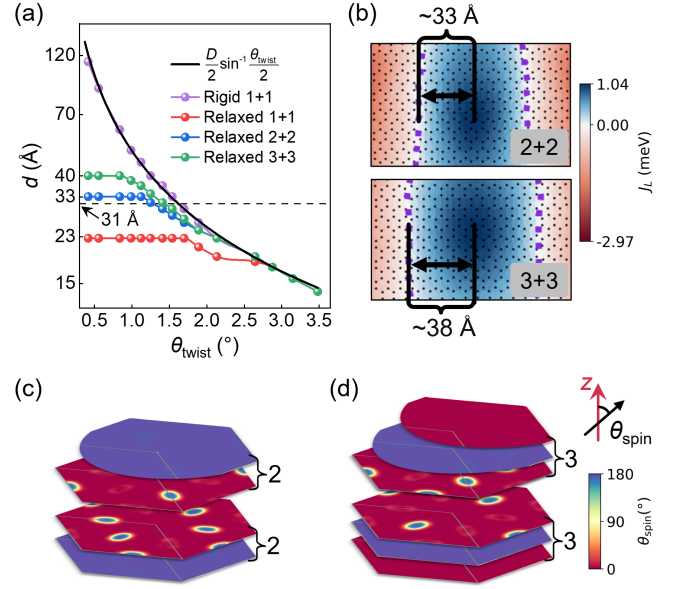


FIG. 3. Tuning of structural relaxation in twisted CrI_3 layers. (a) Evolution of the half-width d of antiferromagnetic J_L region as a function of θ_{twist} for twisted CrI_3 bilayers. Broken line: the threshold to accommodate a magnetic bubble. (b-d) The $\theta_{\text{twist}} = 0.99^\circ$ 2 + 2 and 3 + 3 CrI_3 layers after structural relaxation. (b) Contour maps of J_L . Their d 's are wide enough for magnetic bubbles. (c-d) The corresponding spin textures obtained from simulation.

weaker.

To verify this hypothesis, we investigate the twisted $L + L$ bilayers ($L = 2$ and 3), by keeping the top and bottom L -layer in the M stacking mode as observed in experiment [39, 40]. In these configurations, the interfacial stacking energy E_{stack} remains unchanged, while the strain energy E_{strain} is doubled or tripled compared to that of $L = 1$ case. As a result, the structural relaxation is naturally suppressed in these thick cases, making the relaxed structures and the J_L distributions closer to the rigid lattice model. Therefore, $d > 31$ Å remains a valid criterion to host magnetic bubbles (see Figs. S7-S9 in SM [36]). As compared in Fig. 3(a), larger d 's are reserved for the $L = 2$ and 3 cases, which can go beyond the threshold in the small θ_{twist} limit (1.25° for $L = 2$ and 1.34° for $L = 3$). The simulation patterns of J_L 's distribution confirm this scenario, as shown in Fig. 3(b). As expected, d reaches ~ 33 Å ($L = 2$) and ~ 38 Å ($L = 3$) for the $\theta_{\text{twist}} = 0.99^\circ$ cases. Consequently, the magnetic bubbles indeed appear in these thick twisted bilayers, as shown in Figs. 3(c-d), consistent with the experimental observation of twisted double-bilayer and double-trilayer of CrI_3 [18, 40, 41].

Another interesting observation is that the magnetic bubbles only appear in two interfacial layers, instead of magnetic columns running through the bilayer or trilayer. The number of these 2D bubbles is a constant: three per supercell. Due to the reciprocal relationship between θ_{twist} and the size of supercell, those θ_{twist} 's close to the

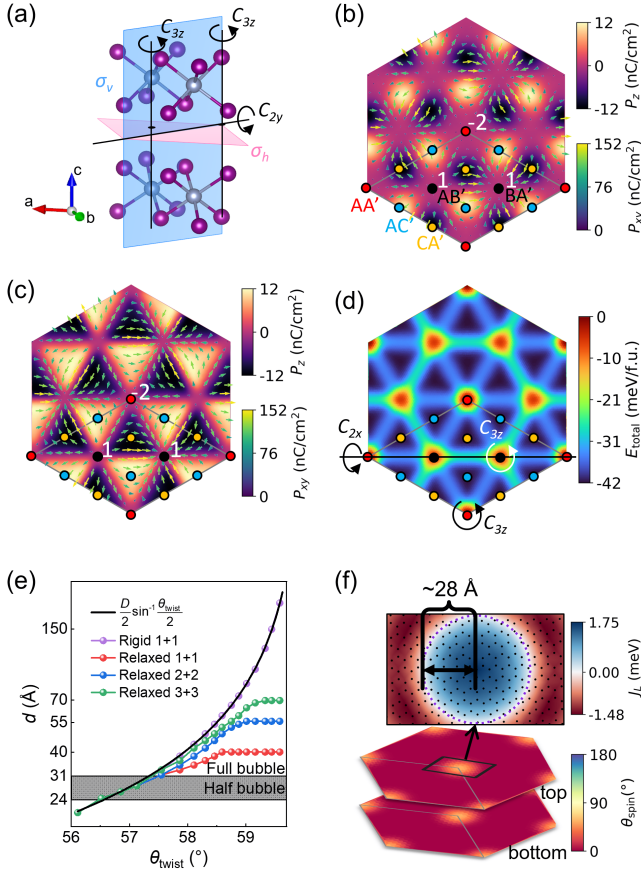


FIG. 4. The $\theta_{\text{twist}} \sim 60^\circ$ twisted (AA'-like) 1 + 1 CrI₃ bilayer. (a) Symmetric elements of the AA' stacking. Ferroelectric textures of the $\theta_{\text{twist}} = 59.01^\circ$ case: (b) without and (c) with structural relaxation. Color dots: the high-symmetric stacking points. Color arrows: the direction of local in-plane electric polarization (P_{xy}), while the out-of-plane component (P_z) is shown as the contour map. The winding numbers (1 & -2) of ferroelectric vortices are indicated. (d) The energy landscape of the $\theta_{\text{twist}} = 59.01^\circ$ case and the symmetric elements. (e) Evolution of d as a function of θ_{twist} for twisted CrI₃. The thicker 2 + 2 and 3 + 3 cases are shown for comparison. (f) Magnetic texture and J_L of the $\theta_{\text{twist}} = 56.85^\circ$ case.

threshold limit can lead to relative high density of magnetic bubbles.

Above study has demonstrated that nontrivial magnetic bubbles as the ground state may survive in the small θ_{twist} limit, while the ground state turns to be plain ferromagnetic when θ_{twist} is slightly large. However, when θ_{twist} is too large, e.g. close to 60° , there is another story of ferroicity. In fact, the $\theta_{\text{twist}} = 60^\circ$ equals to the AA' stacking (i.e. the reversed stacking), which can not be obtained via pure sliding operations from the AA one. In the following, we will study the case with $\theta_{\text{twist}} = (60 - \delta)^\circ$, where δ is a small quantity.

The most interesting physics of reversed stacking is the sliding ferroelectricity, which is absent in the AA one and its derivatives via sliding operations. The 1 + 1 AA' stacking CrI₃ bilayer adopts the noncentrosymmet-

ric non-polar space group $P\bar{6}m2$, and the AB' and BA' ones own the nonpolar space group $P321$ which are obtained by the interlayer sliding along $(1\bar{1}0)$ by $\pm 1/3$ in fractional coordinate. As shown in Fig. 4(a), there are a horizontal mirror (σ_h) plane, three vertical mirror (σ_v) plane, three C_{2y} axes, and two C_{3z} axes in the AA' stacking CrI₃ bilayer. For all other stackings in the AA' \rightarrow AC' \rightarrow CA' \rightarrow AA' path, both P_{xy} and P_z are allowed within the σ_v mirror plane. For sliding perpendicular to the σ_v plane, i.e. along the AA' \rightarrow AB' \rightarrow BA' \rightarrow AA' path, only the C_{2y} axis is preserved. Thus the allowed P_{xy} is aligned along the C_{2y} axis and $P_z = 0$. For any other sliding, the C_{2y} symmetry is broken and both P_z/P_{xy} components are allowed. The distributions of P_z and P_{xy} are summarized in Fig. 4(b). The largest $P_z = 12$ nC/cm² is obtained in the AC'/CA' stackings, while the largest $P_{xy} = 152$ nC/cm² is achieved in the intermediate of AC' \rightarrow CA' path.

The non-polar AA'/AB'/BA' stackings are energetically unfavorable [Fig. 6(b) in EM1], which will lead to structural relaxation. As shown Fig. 4(c), after relaxation, the dominant stacking domains are alternating AC'/CA' ones, and the residual AA'/AB'/BA' modes serve as nodes connected by the AC'/CA' stacking domain walls. Considering the texture of P_{xy} [Figs. 4(b-c)], there are two types of AC'/CA' stacking domain walls: a higher energy one connecting the nearest AB' and BA' nodes; a lower energy one connecting the AA' and AB'/BA' nodes. The ratio of these two domain walls are 1 : 2, as depicted in Fig. 4(d). As the symmetric requirement, all domain walls align parallelly to the C_{2x} axes. Therefore, the polarizations of these stacking domain walls should be along the domain walls with $P_z = 0$.

Around the non-polar AA'/AB'/BA' nodes, ferroelectric vortices are formed in this twisted CrI₃ bilayer, as shown in Figs. 4(d). For the vector field of local dipoles, the AB'/BA' and AA' nodes own non-trivial winding numbers of 1 and -2, respectively. Such topological invariants ensure that the morphology of ferroelectric vortices is highly robust against the structural relaxation, regardless of variations in θ_{twist} , thickness, and electric field (Fig. S10 in SM [36]). Indeed, the 2 + 2 and 3 + 3 twisted CrI₃ exhibit similar ferroelectric vortices (Fig. S11 in SM [36]). The only difference for these thicker cases is that the enlarged volumes reduce the polarizations which originate from the interfacial effect. However, the alternating sign of P_z in AC'/CA' domains leads to zero topological charge for each ferroelectric vortices [see Fig. 9(d) in EM4], different from previously reported topological charge in twisted BN bilayer [26].

For $\theta_{\text{twist}} \sim 60^\circ$, the interlayer magnetic coupling is slightly different from the case of $\theta_{\text{twist}} \sim 0^\circ$. First, the maximum $J_L = 1.72$ meV (AA') is remarkably larger than the largest one ($J_L = 1.04$ meV) of $\theta_{\text{twist}} \sim 0^\circ$ case. As a result, the antiferromagnetic domain centers at the AA' node. Second, the sliding distance from maximum J_L to $J_L = 0$ is longer, leading to a larger $D = 1.44$ Å. Consequently, as shown in Fig. 4(e), θ_{twist} within

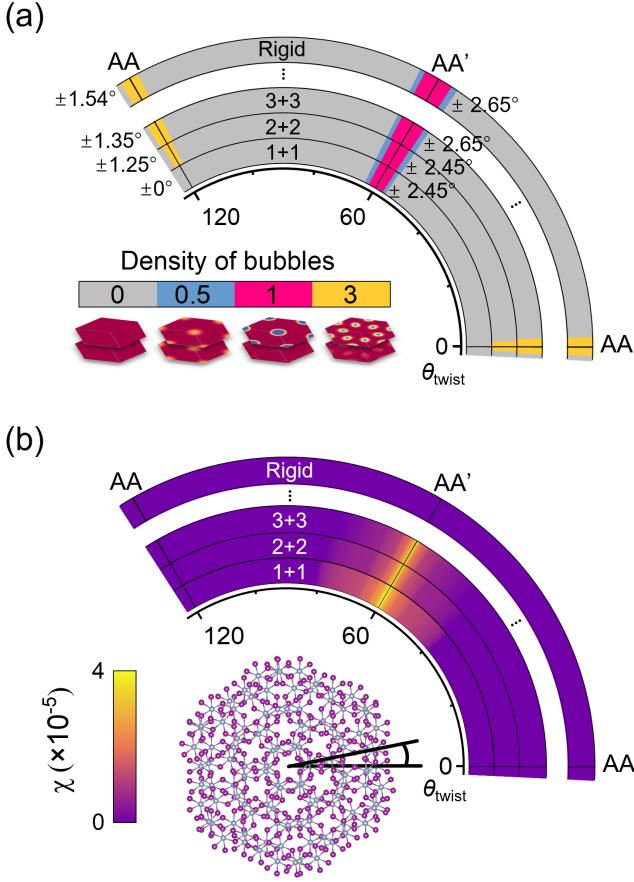


FIG. 5. Summary of magnetic and ferroelectric phase diagram of twisted CrI₃. Evolution of (a) density of magnetic bubbles and (b) susceptibility of twisted CrI₃ superlattices with different θ_{twist} and thickness. Although a net polarization is symmetry-forbidden at zero field, an out-of-plane electric field breaks the balance of stacking domains, leading to a pronounced electric susceptibility ($\chi = \partial P_z / \partial E_z$, E_z : out-of-plane electric field). Larger χ appears when θ_{twist} close to 60° , due to the high proportion of ferroelectric domains.

$60^\circ \pm 2.44^\circ$ can provide sufficient d to accommodate anti-ferromagnetic bubbles in the twisted 1+1 and 2+2 CrI₃. While for the twisted 3+3 and rigidly twisted 1+1 CrI₃, the threshold angles are slightly expanded to $60^\circ \pm 2.65^\circ$. Despite the difference of J_L and D , the threshold d for

antiferromagnetic bubble is almost unchanged, i.e. ~ 31 Å, since it is determined by the intralayer exchange and magnetocrystalline anisotropy.

Another interesting issue is that this larger J_L of $\theta_{\text{twist}} \sim 60^\circ$ can lead to a lower threshold of $d = 24$ Å for half antiferromagnetic bubble [Fig. 4(e)]. For a full antiferromagnetic bubble, the spins rotate for 180° from the edge to the center of a bubble. For a half antiferromagnetic bubble, the spins rotate for 90° from the edge to the center of a bubble. This difference between half bubble and full bubble is analogy to the relation between merons and skyrmions. As shown in Fig. 4(f), the $\theta_{\text{twist}} = 56.85^\circ$ 1+1 CrI₃ bilayer exhibits a $d = 28$ Å half bubble. And the criterion of θ_{twist} for half bubble also applies to the 2+2 and 3+3 cases due to the negligible structural relaxation effect at large δ 's.

To conclude, our study has revealed that the magnetic and ferroelectric properties of twisted CrI₃ layers are finely controlled by the twisting angle θ_{twist} and layer thickness, as summarized in Fig. 5. While the rigid lattice model can provide an initial insight, it fails to capture key results due to the vital contribution from structural relaxation, especially the suppression of magnetic bubbles in thin bilayers. In contrast, the ferroelectric vortices can survive from structural relaxation, thanks to the topological protection. Our results provide a precise theoretical description of ferroicity in twisted materials, paving the way for tailoring nontrivial ferroic orders in twisted vdW materials. Although the present study focused on CrI₃ only, the significance is beyond a single material. The spontaneous lattice relaxation universally exists in all twisted layers, which selectively suppresses or stabilizes different stacking regions according to their energy profiles. Then all physical properties related to stacking modes need to be understood with more realistic models beyond the rigid ones.

ACKNOWLEDGMENTS

This work was supported by National Natural Science Foundation of China (Grant Nos. 12325401 & 12274069) and the Big Data Computing Center of Southeast University.

- [1] B. Huang, G. Clark, E. Navarro-Moratalla, D. R. Klein, R. Cheng, K. L. Seyler, D. Zhong, E. Schmidgall, M. A. McGuire, D. H. Cobden, W. Yao, D. Xiao, P. Jarillo-Herrero, and X. Xu, Layer-dependent ferromagnetism in a van der Waals crystal down to the monolayer limit, *Nature* **546**, 270 (2017).
- [2] C. Gong, L. Li, Z. Li, H. Ji, A. Stern, Y. Xia, T. Cao, W. Bao, C. Wang, Y. Wang, Z. Q. Qiu, R. J. Cava, S. G. Louie, J. Xia, and X. Zhang, Discovery of intrinsic ferromagnetism in two-dimensional van der Waals crystals,

Nature **546**, 265 (2017).

- [3] F. Liu, L. You, K. L. Seyler, X. Li, P. Yu, J. Lin, X. Wang, J. Zhou, H. Wang, H. He, S. T. Pantelides, W. Zhou, P. Sharma, X. Xu, P. M. Ajayan, J. Wang, and Z. Liu, Room-temperature ferroelectricity in CuInP₂S₆ ultrathin flakes, *Nat. Commun.* **7**, 12357 (2016).
- [4] Q. Song, C. A. Occhialini, E. Ergencen, B. Ilyas, D. Amoroso, P. Barone, J. Kapeghian, K. Watanabe, T. Taniguchi, A. S. Botana, S. Picozzi, N. Gedik, and R. Comin, Evidence for a single-layer van der Waals mul-

- tiferroic, *Nature* **602**, 601 (2022).
- [5] P. Man, L. Huang, J. Zhao, and T. H. Ly, Ferroic phases in two-dimensional materials, *Chem. Rev.* **123**, 109906 (2023).
 - [6] M. Yankowitz, J. I.-J. Wang, A. G. Birdwell, Y.-A. Chen, K. Watanabe, T. Taniguchi, P. Jacquod, P. San-Jose, P. Jarillo-Herrero, and B. J. LeRoy, Electric field control of soliton motion and stacking in trilayer graphene, *Nat. Mater.* **13**, 786 (2014).
 - [7] T. Song, X. Cai, M. W.-Y. Tu, X. Zhang, B. Huang, N. P. Wilson, K. L. Seyler, L. Zhu, T. Taniguchi, K. Watanabe, M. A. McGuire, D. H. Cobden, D. Xiao, W. Yao, and X. Xu, Giant tunneling magnetoresistance in spin-filter van der waals heterostructures, *Science* **360**, 1214 (2018).
 - [8] L. Rogee, L. Wang, Y. Zhang, S. Cai, P. Wang, M. Chhowalla, W. Ji, and S. P. Lau, Ferroelectricity in untwisted heterobilayers of transition metal dichalcogenides, *Science* **376**, 973 (2022).
 - [9] T. Song, Z. Fei, M. Yankowitz, Z. Lin, Q. Jiang, K. Hwangbo, Q. Zhang, B. Sun, T. Taniguchi, K. Watanabe, M. A. McGuire, D. Graf, T. Cao, J.-H. Chu, D. H. Cobden, C. R. Dean, D. Xiao, and X. Xu, Switching 2D magnetic states via pressure tuning of layer stacking, *Nat. Mater.* **18**, 1298 (2019).
 - [10] J. Wang, X. Li, X. Ma, L. Chen, J.-M. Liu, C.-G. Duan, J. Iniguez-Gonzalez, D. Wu, and Y. Yang, Ultrafast switching of sliding polarization and dynamical magnetic field in van der waals bilayers induced by light, *Phys. Rev. Lett.* **133**, 126801 (2024).
 - [11] J. Xiao, Y. Wang, H. Wang, C. D. Pemmaraju, S. Wang, P. Muscher, E. J. Sie, C. M. Nyby, T. P. Devereaux, X. Qian, X. Zhang, and A. M. Lindenberg, Berry curvature memory through electrically driven stacking transitions, *Nat. Phys.* **16**, 1028 (2020).
 - [12] Q. Yang and S. Meng, Light-induced complete reversal of ferroelectric polarization in sliding ferroelectrics, *Phys. Rev. Lett.* **133**, 136902 (2024).
 - [13] L. Yang, S. P. Ding, J. H. Gao, and M. H. Wu, Atypical sliding and moiré ferroelectricity in pure multilayer graphene, *Phys. Rev. Lett.* **131**, 136902 (2023).
 - [14] B. Pan, P. Zhou, P. Lyu, H. Xiao, X. Yang, and L. Sun, General stacking theory for altermagnetism in bilayer systems, *Phys. Rev. Lett.* **133**, 166701 (2024).
 - [15] C.-Y. Hao, Z. Zhan, P. A. Pantaleon, J.-Q. He, Y.-X. Zhao, K. Watanabe, T. Taniguchi, F. Guinea, and L. He, Robust flat bands in twisted trilayer graphene moiré quasicrystals, *Nat. Commun.* **15**, 8437 (2024).
 - [16] G. Hu, Q. Ou, G. Si, Y. Wu, J. Wu, Z. Dai, A. Krasnok, Y. Mazor, Q. Zhang, Q. Bao, C.-W. Qiu, and A. Alu, Topological polaritons and photonic magic angles in twisted α -MoO₃ bilayers, *Nature* **582**, 209 (2020).
 - [17] Y. Cao, V. Fatemi, S. Fang, K. Watanabe, T. Taniguchi, E. Kaxiras, and P. Jarillo-Herrero, Unconventional superconductivity in magic-angle graphene superlattices, *Nature* **556**, 43 (2018).
 - [18] T. Song, Q.-C. Sun, E. Anderson, C. Wang, J. Qian, T. Taniguchi, K. Watanabe, M. A. McGuire, R. Stohr, D. Xiao, T. Cao, J. Wrachtrup, and X. Xu, Direct visualization of magnetic domains and moiré magnetism in twisted 2D magnets, *Science* **374**, 1140 (2021).
 - [19] G. Sanchez-Santolino, V. Rouco, S. Puebla, H. Aramberri, V. Zamora, M. Cabero, F. A. Cuellar, C. Munuera, F. Mompean, M. Garcia-Hernandez, A. Castellanos-Gomez, J. Iniguez, C. Leon, and J. Santamaria, A 2D ferroelectric vortex pattern in twisted BaTiO₃ freestanding layers, *Nature* **626**, 529 (2024).
 - [20] K. Yasuda, X. Wang, K. Watanabe, T. Taniguchi, and P. Jarillo-Herrero, Stacking-engineered ferroelectricity in bilayer boron nitride, *Science* **372**, 1458 (2021).
 - [21] S. Shabani, D. Halbertal, W. Wu, M. Chen, S. Liu, J. Hone, W. Yao, D. N. Basov, X. Zhu, and A. N. Pasupathy, Deep moiré potentials in twisted transition metal dichalcogenide bilayers, *Nat. Phys.* **17**, 720 (2021).
 - [22] S. Chen, Z. Liang, J. Miao, X.-L. Yu, S. Wang, Y. Zhang, H. Wang, Y. Wang, C. Cheng, G. Long, T. Wang, L. Wang, H. Zhang, and X. Chen, Infrared optoelectronics in twisted black phosphorus, *Nat. Commun.* **15**, 8834 (2024).
 - [23] S. Carr, D. Massatt, S. B. Torrisi, P. Cazeaux, M. Luskin, and E. Kaxiras, Relaxation and domain formation in incommensurate two-dimensional heterostructures, *Phys. Rev. B* **98**, 224102 (2018).
 - [24] D. Bennett and B. Remez, On electrically tunable stacking domains and ferroelectricity in moiré superlattices, *npj 2D Mater. Appl.* **6**, 7 (2022).
 - [25] M. Akram, H. LaBollita, D. Dey, J. Kapeghian, O. Erten, and A. S. Botana, Moiré skyrmions and chiral magnetic phases in twisted CrX₃ (X = I, Br, and Cl) bilayers, *Nano Lett.* **21**, 6633 (2021).
 - [26] D. Bennett, G. Chaudhary, R.-J. Slager, E. Bousquet, and P. Ghosez, Polar meron-antimeron networks in strained and twisted bilayers, *Nat. Commun.* **14**, 1629 (2023).
 - [27] K. Hejazi, Z. Luo, and L. Balents, Noncollinear phases in moiré magnets, *Proc. Natl. Acad. Sci. U.S.A.* **117**, 10721 (2020).
 - [28] E. Li, J.-X. Hu, X. Feng, Z. Zhou, L. An, K. T. Law, N. Wang, and N. Lin, Lattice reconstruction induced multiple ultra-flat bands in twisted bilayer WSe₂, *Nat. Commun.* **12**, 5601 (2021).
 - [29] A. Weston, Y. Zou, V. Enaldiev, A. Summerfield, N. Clark, V. Zolyomi, A. Graham, C. Yelgel, S. Magorian, M. Zhou, J. Zultak, D. Hopkinson, A. Barinov, T. H. Bointon, A. Kretinin, N. R. Wilsons, P. H. Beton, V. Fal'ko, I. S. J. Haigh, and R. Gorbachev, Atomic reconstruction in twisted bilayers of transition metal dichalcogenides, *Nat. Nanotechnol.* **15**, 592 (2020).
 - [30] N. Tilak, G. Li, T. Taniguchi, K. Watanabe, and E. Y. Andrei, Moiré potential, lattice relaxation, and layer polarization in marginally twisted MoS₂ bilayers, *Nano Lett.* **23**, 73 (2023).
 - [31] H. Yoo, R. Engelke, S. Carr, S. Fang, K. Zhang, P. Cazeaux, S. H. Sung, R. Hoyden, A. W. Tsen, T. Taniguchi, K. Watanabe, G.-C. Yi, M. Kim, M. Luskin, E. B. Tadmor, E. Kaxiras, and P. Kim, Atomic and electronic reconstruction at the van der waals interface in twisted bilayer graphene, *Nat. Mater.* **18**, 448 (2019).
 - [32] Y. Xu, A. Ray, Y.-T. Shao, S. Jiang, K. Lee, D. Weber, J. E. Goldberger, K. Watanabe, T. Taniguchi, D. A. Muller, K. F. Mak, and J. Shan, Coexisting ferromagnetic-antiferromagnetic state in twisted bilayer CrI₃, *Nat. Nanotechnol.* **17**, 143 (2022).
 - [33] J. Ji, G. Yu, C. Xu, and H. J. Xiang, General theory for bilayer stacking ferroelectricity, *Phys. Rev. Lett.* **130**, 146801 (2023).
 - [34] M. A. McGuire, H. Dixit, V. R. Cooper, and B. C. Sales, Coupling of crystal structure and magnetism in the lay-

- ered, ferromagnetic insulator CrI_3 , *Chem. Mater.* **27**, 612 (2015).
- [35] N. Sivadas, S. Okamoto, X. Xu, C. J. Fennie, and D. Xiao, Stacking-dependent magnetism in bilayer CrI_3 , *Nano Lett.* **18**, 7658 (2018).
- [36] See Supplemental Materials for more computational details, including [42–47].
- [37] K.-M. Kim, G. Go, M. J. Park, and S. K. Kim, Emergence of stable meron quartets in twisted magnets, *Nano Lett.* **24**, 74 (2023).
- [38] B. Yang, Y. Li, H. Xiang, H. Lin, and B. Huang, Moiré magnetic exchange interactions in twisted magnets, *Nat. Comput. Ssci.* **3**, 314 (2023).
- [39] G. H. Cheng, M. M. Rahman, A. L. Allcca, A. Rustagi, X. T. Liu, L. N. Liu, L. Fu, Y. Zhu, Z. Mao, K. Watanabe, T. Taniguchi, P. Upadhyaya, and Y. P. Chen, Electrically tunable moiré magnetism in twisted double bilayers of chromium triiodide, *Nat. Electron.* **6**, 434 (2023).
- [40] S. Li, Z. Sun, N. J. McLaughlin, A. Sharmin, N. Agarwal, M. Huang, S. H. Sung, H. Lu, S. Yan, H. Lei, R. Hovden, H. Wang, H. Chen, L. Zhao, and C. R. Du, Observation of stacking engineered magnetic phase transitions within moiré supercells of twisted van der Waals magnets, *Nat. Commun.* **15**, 5712 (2024).
- [41] B. Yang, T. Patel, M. Cheng, K. Pichugin, L. Tian, N. Sherlekar, S. Yan, Y. Fu, S. Tian, H. Lei, M. E. Reimer, J. Okamoto, and A. W. Tsen, Macroscopic tunneling probe of moiré spin textures in twisted CrI_3 , *Nat. Commun.* **15**, 4982 (2024).
- [42] G. Kresse and J. Furthmüller, Efficient iterative schemes for ab initio total-energy calculations using a plane-wave basis set, *Phys. Rev. B* **54**, 11169 (1996).
- [43] J. Perdew, K. Burke, and M. Ernzerhof, Generalized gradient approximation made simple, *Phys. Rev. Lett.* **78**, 1396 (1997).
- [44] S. Grimme, J. Antony, S. Ehrlich, and H. Krieg, A consistent and accurate ab initio parametrization of density functional dispersion correction (DFT-D) for the 94 elements H-Pu, *J. Chem. Phys.* **132**, 154104 (2010).
- [45] S. Dudarev, G. Botton, S. Savrasov, C. Humphreys, and A. Sutton, Electron-energy-loss spectra and the structural stability of nickel oxide: An LSDA+U study, *Phys. Rev. B* **57**, 1505 (1998).
- [46] N. Ding, K. Yananose, C. Rizza, F.-R. Fan, S. Dong, and A. Stroppa, Magneto-optical kerr effect in ferroelectric antiferromagnetic two-dimensional heterostructures, *ACS Appl. Mater. Interfaces* **15**, 22282 (2023).
- [47] R. Kingsmith and D. Vanderbilt, Theory of polarization of crystalline solids, *Phys. Rev. B* **47**, 1651 (1993).
- [48] Y. Sun, S. E. Thompson, and T. Nishida, *Strain Effect in Semiconductors* (Springer Press, New York, 2010).
- [49] B. Berg and M. Lüscher, Definition and statistical distributions of a topological number in the lattice $o(3)$ σ -model, *Nucl. Phys. B* **190**, 412 (1981).

End Matter

EM1. Details of structural relaxation of twisted superlattices. Structural relaxation of the twisted superlattices is done using a lattice model, instead of a direct DFT simulation. The model total energy (E_{total}) is consisted of the interlayer stacking energy (E_{stack}) and intralayer elastic energy (E_{strain}). E_{stack} denotes the change in energy of bilayer CrI_3 as a function of sliding vector \mathbf{u} , which can be obtained via DFT calculation, as shown in Fig. 6(a). For the sliding bilayers, only the out-of-plane coordinates of atoms are optimized in our DFT calculations, while the in-plane coordinates are fixed to avoid the change of sliding vector. As illustrated in Figs. 6(c-d), the local stacking mode in twisted superlattices is approximated to the sliding bilayers. Then, the local stacking energy [Figs. 1(c-d)] can be derived from the sliding energy landscape [i.e. Figs. 6(a-b)]. Similarly, the interlayer magnetic coupling (J_L) and local ferroelectric dipole of twisted CrI_3 are also approximated to the sliding cases.

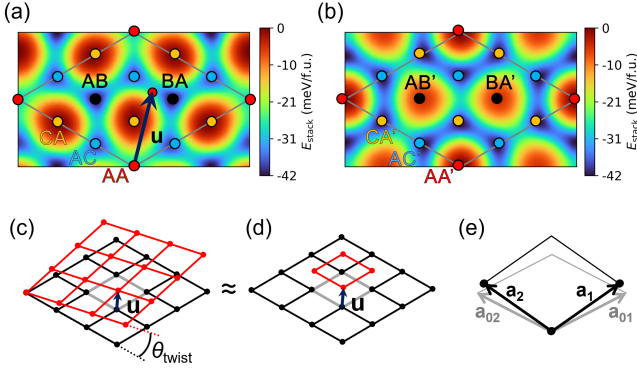


FIG. 6. (a-b) Energy landscape of E_{stack} as a function of sliding vector \mathbf{u} . The original point of sliding vector \mathbf{u} (i.e. $\mathbf{u} = 0$) is (a) the AA stacking one and (b) the AA' stacking one. The highest energy is set as the reference 0 for E_{stack} . (c-d) Correspondence of sliding vector \mathbf{u} 's in the twisted and sliding bilayers. (d) Schematic of local lattice axes \mathbf{a} (in black) and strain-free lattice axes \mathbf{a}_0 (in grey).

The strain tensors (ε) in Eq. 1 can be obtained from [48]:

$$\varepsilon = \mathbf{a}\mathbf{a}_0^{-1} - \mathbf{I} = \begin{bmatrix} \varepsilon_{11} & \varepsilon_{12} \\ \varepsilon_{21} & \varepsilon_{22} \end{bmatrix}, \quad (3)$$

where \mathbf{a} is the local lattice axes and \mathbf{a}_0 is the strain-free lattice axes as shown in Fig. 6(e). \mathbf{I} is the identity matrix. The strain tensor is reshaped to $\varepsilon = [\varepsilon_{11}, \varepsilon_{22}, \varepsilon_{12} + \varepsilon_{21}]$ to match the elastic tensors:

$$C = \begin{bmatrix} C_{11} & C_{12} & 0 \\ C_{21} & C_{11} & 0 \\ 0 & 0 & C_{66} \end{bmatrix}, \quad (4)$$

where $C_{66} = (C_{11} - C_{12})/2$. The elastic tensors are obtained by fitting the energy-strain curves to parabolic

equation of E_{strain} as shown in Fig. S2(a) in SM and the results are listed in Table. S1 in SM [36].

EM2. Details of micromagnetic simulation. In the micromagnetic simulation, the spin dynamics are described by the Landau-Lifshitz-Gilbert (LLG) equation:

$$\frac{\partial \mathbf{S}_i}{\partial t} = -\frac{\gamma}{(1 + \alpha^2)} \mathbf{S}_i \times (\mathbf{H}_{\text{eff}}^i + \alpha \mathbf{S}_i \times \mathbf{H}_{\text{eff}}^i), \quad (5)$$

where α is the Gilbert damping constant, γ is the Gilbert gyromagnetic ratio, and $\mathbf{H}_{\text{eff}}^i = -\frac{1}{\mu_s} \frac{\partial H}{\partial \mathbf{S}_i}$ is the effective field. $\mu_s = 3 \mu_B$ is the magnetic moment of Cr. The LLG equation is solved by the fourth order Runge-Kutta method. $\mathbf{H}_{\text{eff}}^i$ is derived from the Hamiltonian:

$$H = J_{ij} \sum_{\langle i,j \rangle} \mathbf{S}_i \cdot \mathbf{S}_j - K \sum_i (S_i^z)^2 - \frac{\mu_0 \mu_s^2}{4\pi} \sum_{i \neq j} \frac{3(\mathbf{S}_i \cdot \mathbf{r}_{ij})(\mathbf{S}_j \cdot \mathbf{r}_{ij}) - \mathbf{S}_i \cdot \mathbf{S}_j}{r_{ij}^3}, \quad (6)$$

with J and K as the magnetic coupling parameters and the magnetocrystalline anisotropy energy, and the third term is the demagnetization energy.

EM3. Geometric triangulation in twisted superlattices. Eq. 2 stems from the relationship between lattice constants of twisted superlattice (a_{twist}) and unit cell (a_0). As shown in Fig. 7(a), a θ_{twist} twisted superlattice is constructed by two supercells with $\pm\theta_{\text{twist}}/2$. Then, a_{twist} can be obtained according to the geometric triangulation relationship as shown in Fig. 7(b). If a_0 is replaced by the sliding distance (D) between two stacking modes in sliding bilayers (see Fig. 8), the spatial distance (d_{rigid}) between these two stacking modes in the rigidly twisted superlattices is obtained.

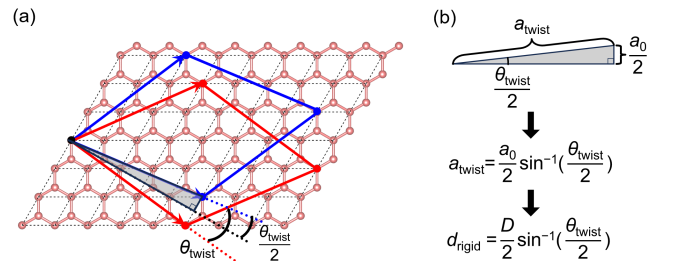


FIG. 7. (a) Schematic of constructing a twisted superlattice. (b) Geometric triangulation relationship between the twisted superlattice and unit cell.

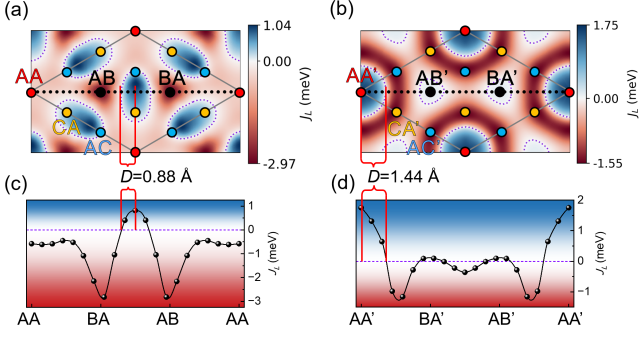


FIG. 8. (a-b) The interlayer magnetic coupling (J_L) of sliding CrI_3 bilayers as a function of sliding vector \mathbf{u} . (a) The AA stacking and its sliding derivatives. (b) The AA' stacking and its sliding derivatives. (c-d) The evolution of J_L 's along the black dash lines in (a-b). D is defined as the half-width of sliding distance corresponding to the antiferromagnetic coupling. Purple broken curve: the $J_L = 0$ boundary.

EM4. Details of topological properties calculations. The winding number ($W_{\mathbf{P}}$) is calculated by the change in azimuth angles (φ) of dipoles around a local site as shown in Fig. 9(a):

$$W_{\mathbf{P}} = \frac{1}{2\pi} \sum_{i=1}^6 (\varphi_{i+1} - \varphi_i), \quad \varphi_7 = \varphi_1. \quad (7)$$

The local topological charge ($q_{\mathbf{P}}$) of polarization is calculated via the solid angles form by four nearest unit cells [49]:

$$q_{\mathbf{P}} = \frac{1}{2\pi} \left[\arg[1 + \mathbf{P}_1 \cdot \mathbf{P}_2 + \mathbf{P}_2 \cdot \mathbf{P}_3 + \mathbf{P}_3 \cdot \mathbf{P}_1 + i\mathbf{P}_1 \times (\mathbf{P}_2 \times \mathbf{P}_3)] + \arg[1 + \mathbf{P}_1 \cdot \mathbf{P}_3 + \mathbf{P}_3 \cdot \mathbf{P}_4 + \mathbf{P}_4 \cdot \mathbf{P}_1 + i\mathbf{P}_1 \times (\mathbf{P}_3 \times \mathbf{P}_4)] \right], \quad (8)$$

where \mathbf{P}_i is the normalized polarization of a local unit cell and a solid angle of a local site is shown in Fig. 9(c).

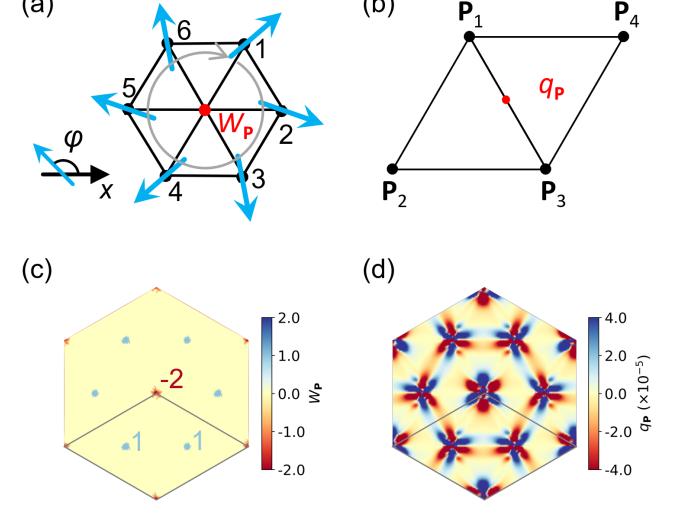


FIG. 9. Definition of (a) azimuth angles φ and (b) topological charge $q_{\mathbf{P}}$. Contour maps of (c) winding number $W_{\mathbf{P}}$ and (d) topological charge $q_{\mathbf{P}}$ of 59.01° 1 + 1 CrI_3 with structural relaxation.